A Simple Cerium Coating Strategy for Titanium Oxide Nanotubes' Bioactivity Enhancement

Serena De Santis [1,*], **Giovanni Sotgiu** [1], **Francesco Porcelli** [1], **Martina Marsotto** [2], **Giovanna Iucci** [2] and **Monica Orsini** [1]

[1] Department of Engineering, Roma Tre University, Via Vito Volterra 62, 00146 Rome, Italy; giovanni.sotgiu@uniroma3.it (G.S.); francesco.porcelli@uniroma3.it (F.P.); monica.orsini@uniroma3.it (M.O.)

[2] Department of Science, Roma Tre University, Via della Vasca Navale 79, 00146 Rome, Italy; martina.marsotto@uniroma3.it (M.M.); giovanna.iucci@uniroma3.it (G.I.)

* Correspondence: serena.desantis@uniroma3.it

Abstract: Despite the well-known favorable chemical and mechanical properties of titanium-based materials for orthopedic and dental applications, poor osseointegration of the implants, bacteria adhesion, and excessive inflammatory response from the host remain major problems to be solved. Here, the antioxidant and anti-inflammatory enzyme-like abilities of ceria (CeO_x) were coupled to the advantageous features of titanium nanotubes (TiNTs). Cost-effective and fast methods, such as electrochemical anodization and drop casting, were used to build active surfaces with enhanced bioactivity. Surface composition, electrochemical response, and in vitro ability to induce hydroxyapatite (HA) precipitation were evaluated. The amount of cerium in the coating did not significantly affect wettability, yet a growing ability to induce early HA precipitation from simulated body fluid (SBF) was observed as the oxide content at the surface increased. The presence of 4%wt CeO_x was also able to stimulate rapid HA maturation in a (poorly) crystalline form, indicating an interesting potential to induce rapid in vivo osseointegration process.

Keywords: titanium; cerium oxide; nanotubes; bioactivity

1. Introduction

Titanium (Ti)-based materials are widely used for orthopedic and dental implants thanks to their favorable mechanical properties, corrosion resistance in body fluids, and excellent biocompatibility [1]. However, titanium-based implants are often reported to be subject to long term complications, mostly related to loosening of the implant–host interface and susceptibility of the implant to bacterial infections [2]. Poor osseointegration is the basis of both phenomena. As a bio-inert material, Ti is not able to actively interact with the surrounding environment and to favor a satisfactory cell adhesion, which are instead key points for the formation of the structural and functional direct connection between the living bone and the implant surface needed to ensure long-term stability [3]. Great efforts have been paid to improve bone–implant contact, such as changing the substrate surface topography [4,5], chemically modifying the surface layer [6,7], and coating the implant with bioactive materials [8,9]. Fabricating a TiO_2 nanotube array (TiNT) by means of direct electrochemical anodic oxidation of the titanium substrate is one of the most promising approaches. This porous oxide layer, tightly bonded to the bulk material, proved able to establish beneficial interactions with osteogenic cell types, in terms of adhesion and differentiation, while limiting bacterial attachment [10,11]. In vitro studies also indicated that TiO_2 nanostructures could be used as smart delivery systems in implants, thus enabling the possibility of releasing active molecules, such as antibiotics or loaded polymer micelles, directly at the site of implantation [12,13]. Nanotubes' length, diameter, and composition can be easily controlled by varying the processing parameter, and highly reproducible and homogeneous surfaces can be obtained.

The immune response is a further concern to be considered. Although inflammation is a natural and important stage of the wound healing process in which damaged cells, pathogens, and bacteria are removed from the wound area, prolonged or excessive inflammatory conditions can impair bone remodeling [14]. The oxidative stress which accompanies inflammation, with overproduction of harmful reactive oxygen species (ROS), is known to be responsible for inducing apoptosis of the osteoblastic cell line and inhibiting osteoblast differentiation, finally leading to bone loss [15]. Thus, imparting antioxidant function to the biomaterial is a crucial point to prolong the service life of implants. Therefore, the three key factors prompting the clinical success of an implant are ensuring rapid osseointegration, reducing inflammation around the implant, and preventing bacterial adherence on the implant surface.

Metal elements such as silver (Ag), gold (Au), copper (Cu), zinc (Zn) [16,17] or combinations thereof and with hydroxyapatite [18,19] have been thoroughly examined as titanium-based material enhancers to improve their antibacterial activity. Strontium (Sr) and silicon (Si) have also been considered as essential trace elements in biological processes [20]. More recently, ceria (CeO_2), one of the most reactive rare-earth metal oxides, has received growing attention in biomedical applications due to its unique physical and chemical properties and reported biocompatibility [21–23]. Nanoceria was recently found to have superoxide dismutase, catalase, and oxidase mimetic properties, possessing ROS-scavenging capability comparable to those of biological enzymes [24]. Such characteristic functionalities depend on the presence of mixed valence states (Ce^{3+} and Ce^{4+}) and oxygen vacancies that allow this redox couple to rapidly switch between the two forms according to the conditions of the immediate environment [25]. The multiple enzyme activities of CeO_2 can be exploited to introduce promising antibacterial and anti-inflammatory properties. Ceria has been successfully evaluated in bone regenerative biomaterials as a pure coating [26,27], integrated component [28,29], and nanoparticulated material [30,31], not only confirming its protective capability but also positively influencing the osteogenic activities of bone marrow mesenchymal stem cells (BMSCs) [32]. The aim of the present work was to propose a very simple coating procedure which could eventually be readily transferred into industrial and then clinical applications. With this purpose, a mixed oxide ceria ceramics (CeO_x) coating onto anodized titanium substrates (TiNT) is realized, employing the drop casting method, a simple and cost-effective deposition method, which allowed for good control over the cerium surface percentage. The effect of varying cerium content is examined, looking for the lowest quantity capable of producing a significant bioactivity enhancement in terms of hydroxyapatite inducing ability.

2. Materials and Methods

2.1. Samples Preparation

TiO_2 nanotube arrays (TiNT) were obtained by a one-step anodization process from commercially pure titanium foil (thickness 0.127 mm, 99.7% trace metals basis, Merk Life Science, Milano, Italy). Samples were degreased by ultrasonic cleaning in water/acetone 50:50 and ethanol for 10 min, rinsed with deionized water, and dried under an air stream at ambient temperature. Anodic oxidation was performed under potentiostatic control (15 V, 45 min), using 1 cm × 1.5 cm cleaned Ti foils as working electrodes and a platinum wire as a counter electrode. The two electrodes were placed in an electrolyte consisting of H_2O/glycerol 40:60 with 0.25 wt% NH_4F (≥99.99% trace metals basis, Merk Life Science, Milano, Italy). Anodized samples were thoroughly rinsed with deionized (DI) water and air dried. Cerium-coated samples (TiNT_Ce) were obtained by the drop casting technique, repeatedly depositing 20 μL of a 10^{-2} M $Ce(NO_3)_3 \cdot 6H_2O$ (99.99% trace metals basis, Merk Life Science, Milano, Italy) solution in ethanol. Each deposition was followed by a 10 min annealing step at 400 °C; in the final step, samples were annealed for 2 h at 400 °C and left to cool to an ambient temperature. Five samples were prepared, named $TiNT\_Ce_n$, with n being 1, 3, 6, 9, and 12 respectively, based on the number of depositions performed.

2.2. Surface Characterization

Morphological and compositional observations of the samples were obtained by scanning electron microscopy with energy dispersive X-ray spectroscopy (SEM-EDS) using a Zeiss Gemini SIGMA 300 FEG SEM (Jena, Germany) equipped with Bruker EDS (Bruker Italia, Milano, Italy). Micrographs were obtained at 5 kV, while EDS analysis was performed at an accelerating voltage of 20 kV, with a back scattered detector and working distance of 7.5 mm.

XPS analysis was performed with a homemade instrument, consisting of preparation and analysis UHV chambers separated by a gate valve. The analysis chamber is equipped with a six-degree-of freedom manipulator and a 150 mm mean radius hemispherical electron analyzer with a five-lens output system combined with a 16-channel detector, giving a total instrument resolution of 1.0 eV as measured at the Ag $3d_{5/2}$ core level. Samples were introduced in the preparation chamber and left outgassing overnight at a base pressure of about 10^{-8} Torr, before introduction in the analysis chamber. Typical vacuum pressure in the analysis chamber during measurements was in the 10^{-8}–10^{-9} Torr range. The used X-ray radiation was a non-monochromatized Mg $K\alpha$(1253.6 eV). The spectra were energy referenced to the Ti $2p_{3/2}$ signal of titania nanotubes having a binding energy BE = 458.50 eV. Atomic ratio values were calculated from peak intensities. Curve-fitting analysis of the C 1s, N 1s, O 1s, Ti 2p and Ce 3d spectra was performed using Gaussian profiles as fitting functions, after subtraction of a Shirley-type background. $Ti2p_{3/2,1/2}$ and $Ce3d_{5/2,3/2}$ doublets were fitted by using the same Full Width at Half-Maximum (FWHM) for each pair of components of the same core level, a spin–orbit splitting of, respectively, 5.7 and 18.3 eV and branching ratios $Ti2p_{3/2}/Ti2p_{1/2}$ =2/1, $Ce3d_{5/2}/Ce3d_{3/2}$ =3/2.

2.3. Electrochemical Measurements

Corrosion characteristics of the coated samples were investigated using the potentiodynamic polarization test using an AMEL System 5000 workstation (AMEL, Milano, Italy), CorrWare software version 3.5c (Scribner, NE, USA) for the acquisition and CorrView software version 3.5c (Scribner, NE, USA) for the elaboration. Measurements were performed on 1 cm^2 samples areas at 37 °C using a simulated body fluid (SBF) as an electrolyte in a three-electrode electrochemical cell with the TiNT or $TiNT\_Ce_n$ sample as the working electrode (WE), a platinum wire as a counter electrode (CE), and Ag/AgCl as the reference electrode. The polarization tests were conducted at a scan rate of 10 mV/s vs. open circuit potential (OCP) in the potential range −400–500 mV.

Electrochemical impedance spectroscopy (EIS) was recorded using a Solartron 1255B Frequency Response Analyzer (AMETEK Scientific Instruments, Milano, Italy). The frequency ranged from 60 kHz to 100 mHz, with an ac amplitude of ±10 mV. Before measurement, samples were immersed in the SBF electrolyte at 37 °C until the open circuit reached a steady-state value. EIS data were analyzed considering equivalent electrical circuits using the ZView fitting program (Scribner, NE, USA). Reproducibility of the results was confirmed by repeating each measurement at least three times.

SBF was prepared according to the standard procedure proposed by Kokubo et al. [33]. The solution composition is reported in Table 1; the final pH was 7.41. All reagents were purchased from Merk Life Science (Milano, Italy) and used as received.

2.4. Surface Wettability

Surface wettability was investigated through water contact angle (WCA) measurements carried out using homemade contact angle meter equipment realized with respect to the relative normative (UNI EN 828, UNI 9752, ASTM D-5725-99). Three samples were observed for each condition, depositing four drops (3 µL) on each; the corresponding image was captured with an Olympus Software Imaging System after 20 s stabilization. The contact angle was measured using ImageJ software.

Table 1. Ion concentration in simulated body fluid (SBF) solution.

Ion	Ion Concentrations (mM)
Na^+	142.0
K^+	5.0
Mg^{2+}	1.5
Ca^{2+}	2.5
Cl^-	147.8
HCO^{3-}	4.2
$HPO_4{}^{2-}$	1.0
$SO_2{}^{4-}$	0.5

2.5. In Vitro Bioactivity Test

Bioactivity was evaluated upon immersion in SBF, following the standard procedure described by the International Standard ISO 23317:2014 [34]. Samples were placed in sterilized tubes filled with SBF which were then sealed and placed in a thermostatic bath at 37 °C for 8 days. Samples were then thoroughly rinsed with DI water and air dried prior to subsequent analysis. The formation of calcium-phosphate species (CaPs) was assessed by EDS analysis, while identification of their type was obtained by Fourier transformed infrared (FT-IR) microspectroscopy, using a Nicolet iN10 infrared microscope (Thermo Fisher Scientific IT, Milano, Italy) equipped with a mercury-cadmium-telluride (MCT-A) nitrogen-cooled detector in ATR mode. The FTIR spectra were collected in the 4000–650 cm^{-1} range as an average of 64 scans, with 8 cm^{-1} resolution. At least five measurements were acquired from different areas for each sample. OmnicPicta software version 2.03 (Thermo Fischer Scientific, Milano, Italy) was used for post elaboration of the spectra.

3. Results and Discussion

The morphology, surface composition, and electrochemical behaviour of $TiNT\_Ce_n$ (obtained by titanium anodization at 15 V followed by drop casting deposition of a cerium precursor solution and heat treatment at 400 °C) were analysed in detail.

3.1. Surface Morphology and Composition

The FE-SEM micrographs of the pristine and ceria-coated titanium nanotube samples are given in Figure 1a–f. A uniform and regular distribution of the stacked, unidirectional nanotube array can be observed over the substrate.
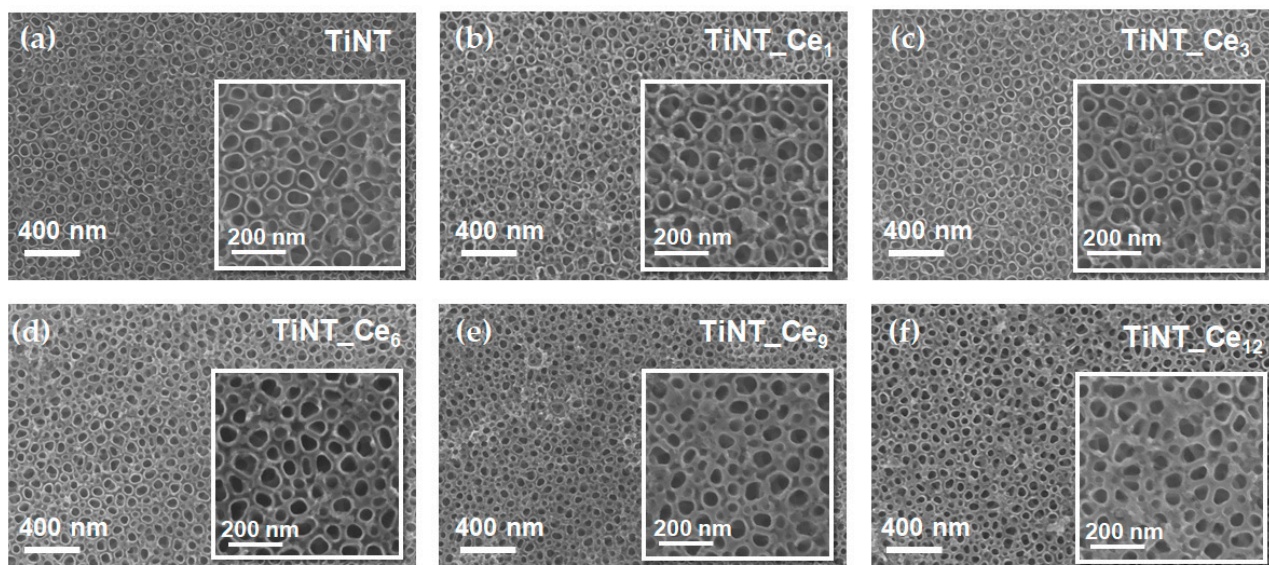
Figure 1. Top surface FE-SEM images of (**a**) TiO_2 nanotube and (**b–f**) cerium-coated TiO_2 nanotubes with increasing amount of CeO_2.

The pristine titania nanotubes are approximately 50 nm in diameter (Figure S1). SEM micrographs suggest that when the $Ce(NO_3)_3$ solution is drop casted onto the surface, cerium ions are mainly deposited on interstices. In fact, as the number of solution depositions increased, the outer diameter of the tubes progressively rose, while the inner diameter was substantially maintained. The cerium oxide layer preferentially occupies the void space between nanotubes, providing a higher nanostructure surface density while preserving the open top nanotubular pattern. The thickening of the nanotube walls is almost negligible for the lower cerium content considered, while it becomes more important for the samples TiNT_Ce$_9$ and TiNT_Ce$_{12}$. The original inner size of the nanotubes, which can be finely tuned by choosing the proper parameters during anodization process, is maintained (Figure S1). This is an important feature, since it was demonstrated that TiO_2 nanotube diameter strongly affects osteogenic cell adhesion, growth, and differentiation [35].

Energy dispersive X-ray spectroscopy (EDS) analysis confirms the presence of cerium on all samples surfaces with a percentage varying between 0.8 and 8%, going from TiNT_Ce$_1$ to TiNT_Ce$_{12}$, respectively (Figure S2, Table S1).

X-ray photoelectron spectroscopy (XPS) measurement on TiNT_Ce$_n$ samples was carried out at the C 1s, O 1s, Ti 2p and Ce 3d core levels (Figure 2, Figures S3 and S4). Pristine titania nanotubes, anodized in the same conditions, were also measured; the obtained data were used as standard for the interpretation of the signals arising from the coated specimens. Ti2p spectra (Figure S4) are made of one spin-orbit doublet (Ti2p$_{3/2}$, Ti2p$_{1/2}$). The Ti2p$_{3/2}$ signal at 458.5 eV, taken as reference for the Ti2p$_{3/2-1/2}$ spin−orbit pair, is associated to titania nanotubes and so attributed to fully oxidized Ti^{4+} species [36]. It is thus possible to infer that the Ce^{3+} ions of the precursor solution do not interact directly with titanium atoms but rather form Ti-O-Ce bridges, as already observed by other authors [22,37].
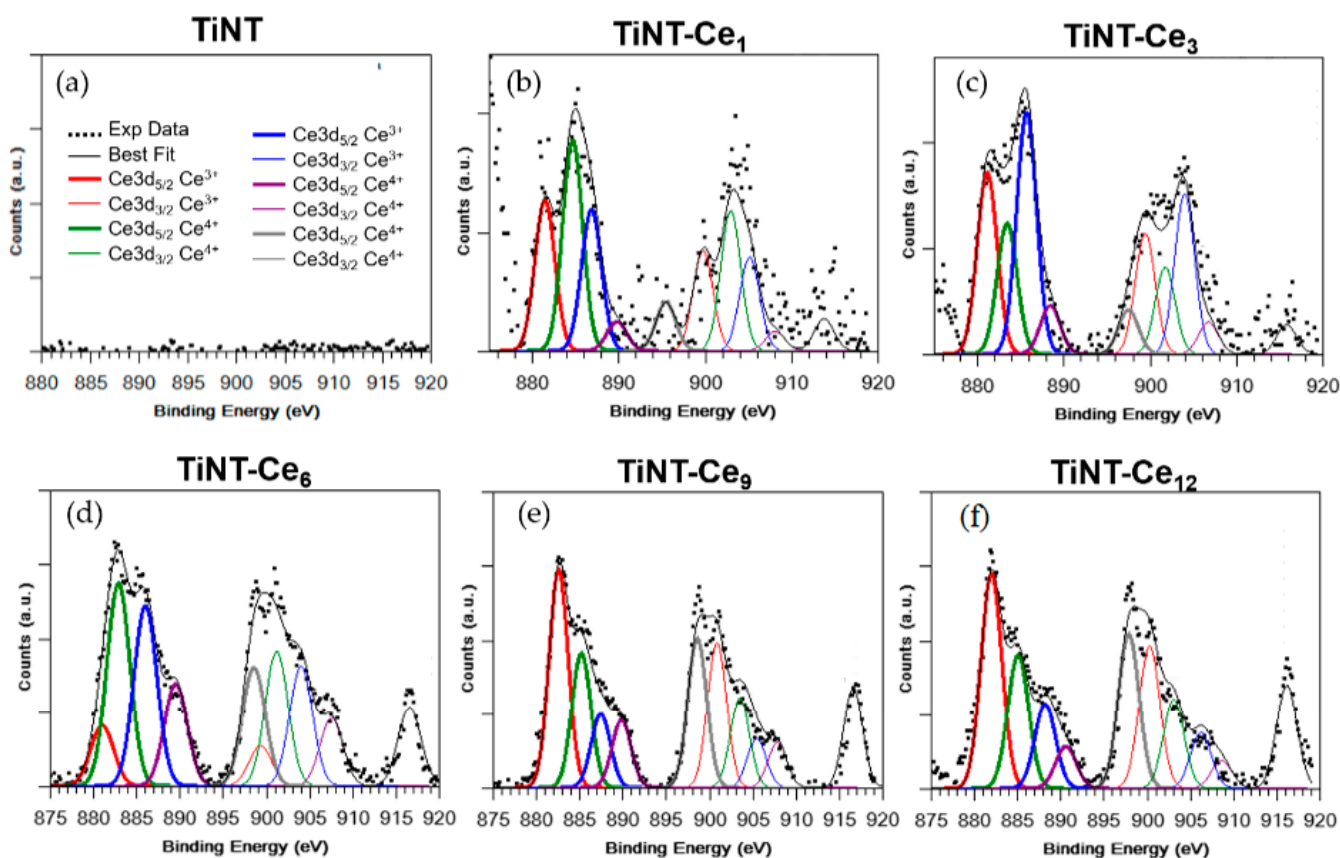
Figure 2. XPS Ce3d fitted spectra for the (**a**) TiO_2 nanotube (TiNT) and (**b**–**f**) cerium-coated (TiNT_Ce$_n$) samples.

By following a peak-fitting procedure, five spin orbit pairs related to Ce3d were individuated (Figure 2), and the resulting components were associated with Ce^{3+} and Ce^{4+} species by comparison with literature data [38]. The intensity of the $Ce3d_{3/2}$ signal at higher binding energy, which indicates the amount of ceria in the sample, increased from $TiNT\_Ce_1$ to $TiNT\_Ce_{12}$, as expected. The Ce^{3+}/Ce^{4+} ratio can control the enzyme-like behavior of the oxide [27]; this ratio was estimated for every sample considering the total contribution of each species, comparing the area associated with the Ce^{3+} peaks with the total area of the Ce3d spectrum signals. The data showed that an approximately 1:1 ratio mixture of Ce^{3+} and Ce^{4+} was formed by the deposition procedure comprising extensive heat treatment in air. Ce^{4+} coatings exert greater anti-inflammatory effects and proved more efficient at enhancing the osteogenic activities of BMSCs [27]. At the same time, the ability to preserve large amount of reduced cerium atoms is quite important, since in this form, it exhibits the highest ability to bind phosphate species [39].

3.2. Electrochemical Behavior

Potentiodynamic polarization studies for the TiNT and cerium-coated samples were performed to gain information about the polarization domains of these surfaces in SBF solution (Figure 3). All samples were immersed in the electrolyte for 2 h to ensure stabilization of OCP before all experiments.
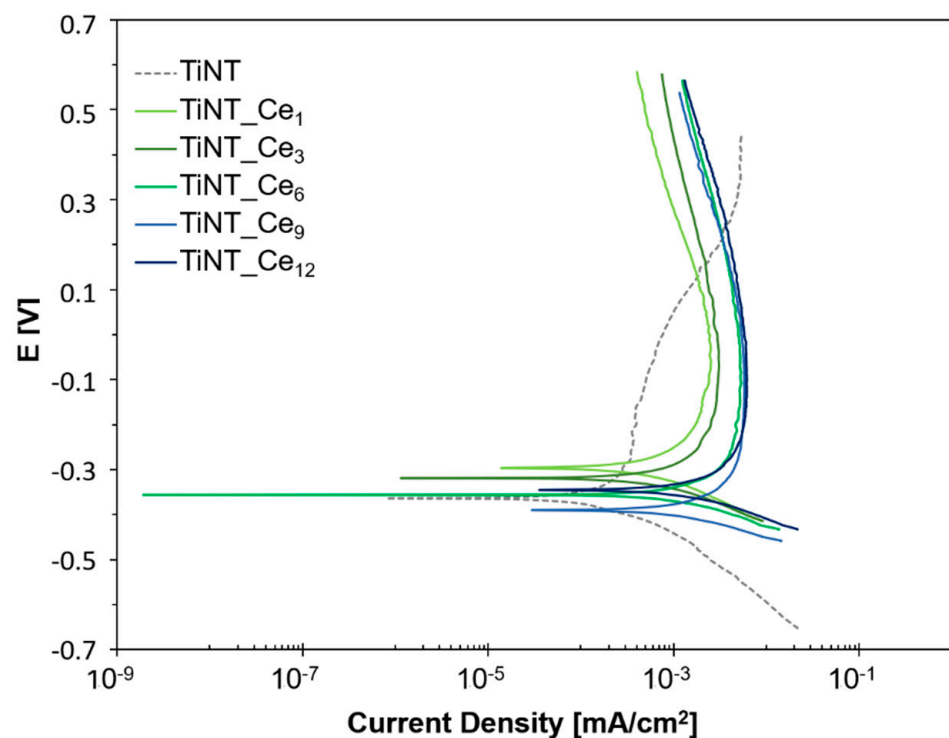
Figure 3. Potentiondynamic polarization curves for TiNT and $TiNT\_Ce_n$ samples recorded in SBF at 37 °C.

The kinetic parameters obtained by potentiodynamic polarization curve analysis are given in Table 2.

Table 2. Electrochemical parameters of the titanium and cerium-coated samples measured in SBF at 37 °C.

	E_{corr} (V)	I_{corr} (µA)	$I_{pass-0.2}$ (µA)	$I_{pass0.3}$ (µA)
TiNT	−0.364	0.57	0.37	4.87
TiNT_Ce$_1$	−0.297	1.70	1.83	0.95
TiNT_Ce$_3$	−0.320	1.36	2.81	1.48
TiNT_Ce$_6$	−0.356	3.18	5.72	3.16
TiNT_Ce$_9$	−0.396	3.18	5.87	3.18
TiNT_Ce$_{12}$	−0.345	3.93	5.87	3.26

$I_{pass-0.2}$ and $I_{pass0.3}$: current at a potential of −0.2 and 0.3 V, respectively.

The I_{corr} and E_{corr} of each sample ranged from 0.57 to 3.93 µA/cm^2 and from −0.396 to −0.297 V, respectively. The almost corresponding active potential of all the samples suggests very similar corrosion susceptibility in terms of E_{corr}. A broad passive domain was quickly formed starting from −0.2 V for all the considered samples, with values of I_{pass} quite similar to those of I_{corr}, indicating that the protective behavior is rapidly established. At potential higher than − 0.2 V, the current density of TiNT_Ce$_n$ samples showed almost no change with the increase in the potential, except for a constant slight decrease, indicating the formation of a stable oxide layer, which is effective against further corrosion over a wide potential. The uncoated nanotube sample showed an apparent lower I_{pass} value; however, an unstable passive layer is formed in that case. As indicated by the dashed gray line, a continuous increase in the current value is observed until a potential of 0.3 V is reached, at which the current value is higher than for any other TiNT_Ce$_n$ sample. These results indicate that cerium-coated samples have good corrosion resistance. The constant behavior at increasing potential suggests that there are no significant mass losses or debris formation from the surface of TiNT_Ce$_n$ during the corrosion process, which makes coated samples safer with respect to toxic effects induced by metal leakage.

To further characterize the properties of cerium-coated titanium nanotubes, electrochemical impedance spectroscopy (EIS) measurements were carried out (Figure 4). The obtained spectra were interpreted using an equivalent electrical circuit model consisting of a solution resistance (R_{el}) in series with a parallel circuit of constant phase element (CPE) and charge transfer resistance (R_{ct}).
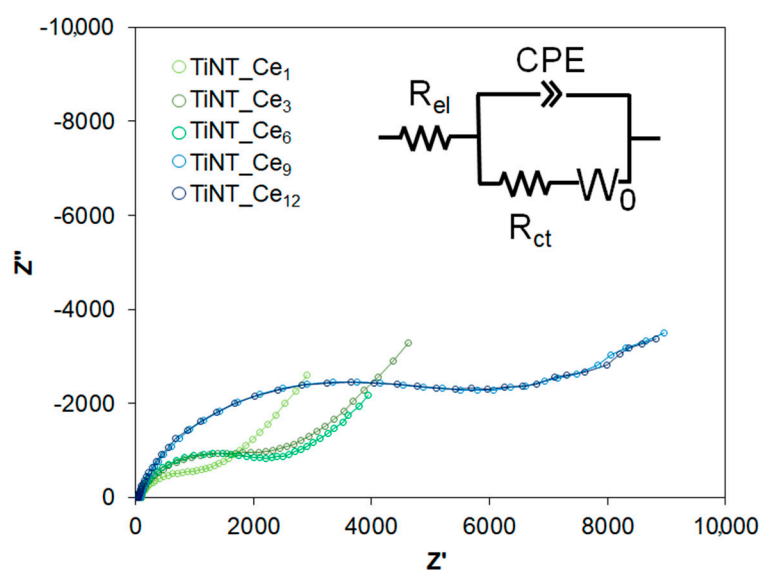
Figure 4. Electrochemical impedance spectroscopy (EIS) spectra of ceria deposited TiNT samples. Empty circles correspond to experimental data, solid lines indicate the corresponding fit. The equivalent circuit used is also represented.

The use of a CPE instead of a pure capacitance accounts for the non-homogeneous double layer formed by the nanotubular structure. Because of the diffusional phenomenon observed in the low frequency regime of the Nyquist spectrum, which may be due to the ingress of ionic species within the nanotubular structure of oxide film, an additional Warburg element in series with R_{ct} was also considered. Fit results are summarized in Table 3; χ^2 values of 10^{-3}–10^{-4}, obtained for all the parameters, indicate very good agreement between the experimental data and the simulated values.

Table 3. Electrochemical parameters obtained from the equivalent circuits of the TiNT_Ce$_n$ samples by measuring the open circuit potential (OCP) at 37 °C using SBF as the electrolyte.

| | R_{el} $(\Omega \cdot cm^2)$ | $R_{ct}(k\Omega \cdot cm^2)$ | CPE | | σ $(k\Omega \cdot s^{-1/2} \cdot cm^{-2})$ | χ^2 |
			Y_o $(\mu S \cdot s^n \cdot cm^{-2})$	n		
TiNT_Ce$_1$	82.6	0.56	10.48	0.892	2.44	$1.00 \cdot 10^{-3}$
TiNT_Ce$_3$	77.0	1.32	5.29	0.881	4.64	$1.00 \cdot 10^{-4}$
TiNT_Ce$_6$	69.6	1.81	5.43	0.876	4.95	$1.00 \cdot 10^{-4}$
TiNT_Ce$_9$	84.4	2.82	4.76	0.880	10.47	$1.00 \cdot 10^{-4}$
TiNT_Ce$_{12}$	70.2	3.55	3.75	0.884	11.40	$1.00 \cdot 10^{-3}$

The charge relaxation coefficient (n) gave information about the non-uniform distribution of charge at the surface of the electrode. The charge distribution characteristics of oxide film were quite similar for all TiNT_Ce$_n$ samples, as only minor differences were found in the n values for each sample (Table 3). However, the diminishing value of constant phase element admittance Y_o (10.48 to 3.75 $\mu S \cdot s^n cm^{-2}$) going from TiNT_Ce$_1$ to TiNT_Ce$_{12}$ revealed lower charge dissipation in redox reactions induced by the increase in CeO$_x$ content on the surface. This observation suggests that ceria depositions actively contribute to give good barrier characteristics to the surface, exerting a blocking effect toward titanium active sites, as already observed for similar systems obtained by electrodeposition of CeO$_x$ on TiNT [22]. The improvement in the barrier properties of surface oxide film was further validated by the higher charge transfer resistance values growing from 0.56 to 3.55 k$\Omega \cdot cm^2$.

The Warburg element in the circuit represents the semi-infinite linear diffusion through the surface and, in our case, it is also related to the transport of ionic species of the electrolyte trough the nanotubular structure. The Warburg coefficient, σ, can give information about the ease with which ions could reach the substrate to react. A progressive increase in σ values was observed with increasing amounts of ceria on the surface, going from 2.44 k$\Omega \cdot s^{-1/2} \cdot cm^{-2}$ for a single cerium ion deposition to 11.40 k$\Omega \cdot s^{-1/2} \cdot cm^{-2}$ for TiNT_Ce$_{12}$, indicating a lower susceptibility of the surface to ion transport, lowering the risk of corrosion reactions.

3.3. Surface Wettability

Surface wettability plays a major role in determining biomaterial interactions with the physiological surrounding, affecting protein and macromolecules adsorption, cell and bacterial adhesion, and the in vivo rate of osseointegration [40]. Samples' surface wettability was assessed by measuring their contact angle (θ) with water droplets. The contact angle of TiNT was 22.1° ± 2.2°; cerium-coated samples showed values of θ between 29.1° ± 1.7° and 34.8° ± 2.1° (Figure 5), with a slight decrease in wettability caused by CeO$_x$, apparently not proportional to the cerium content. The increase in θ due to cerium was already observed in the literature, and it was connected to a decrease in the active sites on the titanium surface due to the replacement of -OH groups with O-Ce bonds [22]. Nevertheless, the low values of θ indicate a still highly hydrophilic behaviour of the coating which can favour the ion exchange from the body fluids and interactions with proteins. In fact, the good hydrophilicity of nanotube arrays is known to be related to their special structure which is maintained by the coating procedure adopted and seems to exert the predominant effect.
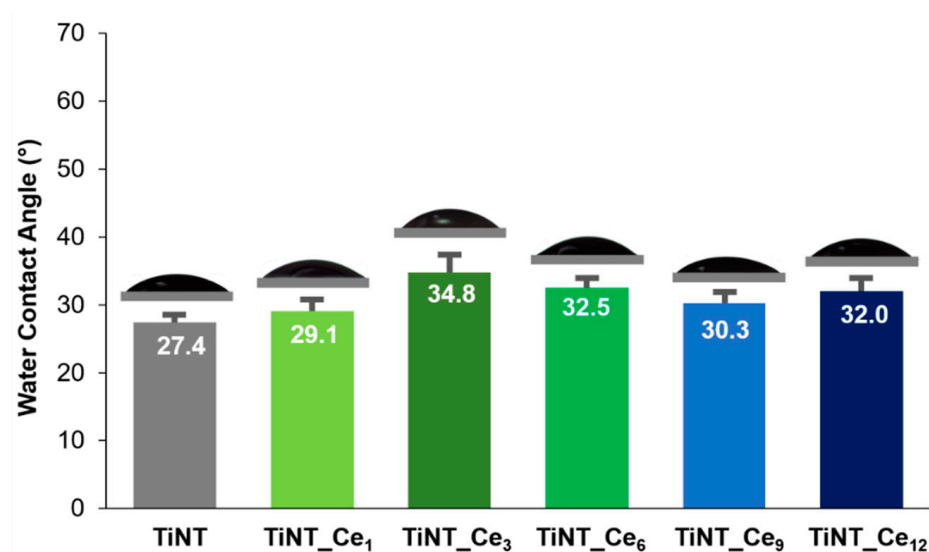
Figure 5. Water contact angle measurements.

3.4. In Vitro Bioactivity

The integration of biomaterials is crucial to ensure long-term stability of the implant. For a successful bond with tissue to occur, the formation of a layer of biologically active hydroxyapatite (HA) is needed. The mineralization process of calcium phosphates in bone starts from an amorphous calcium-phosphate (CaP) precursor phase which turns into nanocrystalline carbonated HA as a result of an autocatalytic process [41]. It was established that the ability of a material to form a CaP layer in a simulated body fluid, without the support of the protein and cellular components characteristic of the in vivo process, is largely predictive of good bioactive behavior [42]. Thus, the HA forming ability of $TiNT\_Ce_n$ samples in SBF at 37 °C was investigated. The SEM micrographs after 8 days soaking are shown in Figure 6. Only a low amount of precipitate was found in TiNT micrographs in such a short time (Figure 6a), as already observed in the literature [22]. Instead, all the cerium-coated samples were capable of inducing a significant early apatite-like species growth. In greater detail, a relationship between the cerium surface content and the ability of favoring apatite nucleation is clearly visible (Figure 6b–e). A progressively more compact HA layer is found from $TiNT\_Ce_1$ to $TiNT\_Ce_{12}$, with the latter achieving a complete covering, hiding the underlying nanotubular structure.

The EDS spectra confirmed that Ca and P species are present on the surface, with the elements uniformly distributed along the whole specimen (Figure S5). A Ca/P atomic ratio between 1.42 and 1.57, compatible with non-stoichiometric, calcium-deficient HA, was detected (Table S2). For a deeper investigation of the nature of the Ca/P phase, the ATR-FTIR spectra of $TiNT\_Ce_n$ were also recorded (Figure 7).

The typical ν_1 and ν_3 vibrational mode of phosphate (PO_4^{3-}) bands of apatite were detected at 956, 1055, and 1101 cm^{-1} respectively. The presence of carbonate species was also revealed by the relative bands at 1422 and 1446 cm^{-1}. These observations are consistent with carbonate-substituted hydroxyapatite (CHA), with carbonate ions replacing phosphate and/or hydroxyl positions, respectively [43]. CHA is the actual main component of dental and bone tissues in humans and it is known to have an impact on different pathologies [44, 45]. It is important to note that CHA is more soluble than HA, thus increasing the local concentration of Ca and P ions and accelerating new bone formation.

The shape and resolution of the ν_3 PO_4^{3-} bands can give qualitative indication about the crystallinity of the HA coating [46]. For lower CeO_x content samples, a single broad signal was observed (Figure 7b), indicating that the HA phase is essentially amorphous. Starting from $TiNT\_Ce_6$, a shoulder is clearly recognizable, becoming more prominent as the amount of CeO_x on the surface grows, thus indicating a poorly crystalline type of HA.

Taken together, the EDS and FTIR results indicate that the presence of cerium on the surface promotes early calcium phosphate species precipitation and, as a function of its concentration, accelerates the maturation of the HA phase, actively favoring the osteointegration process [47].
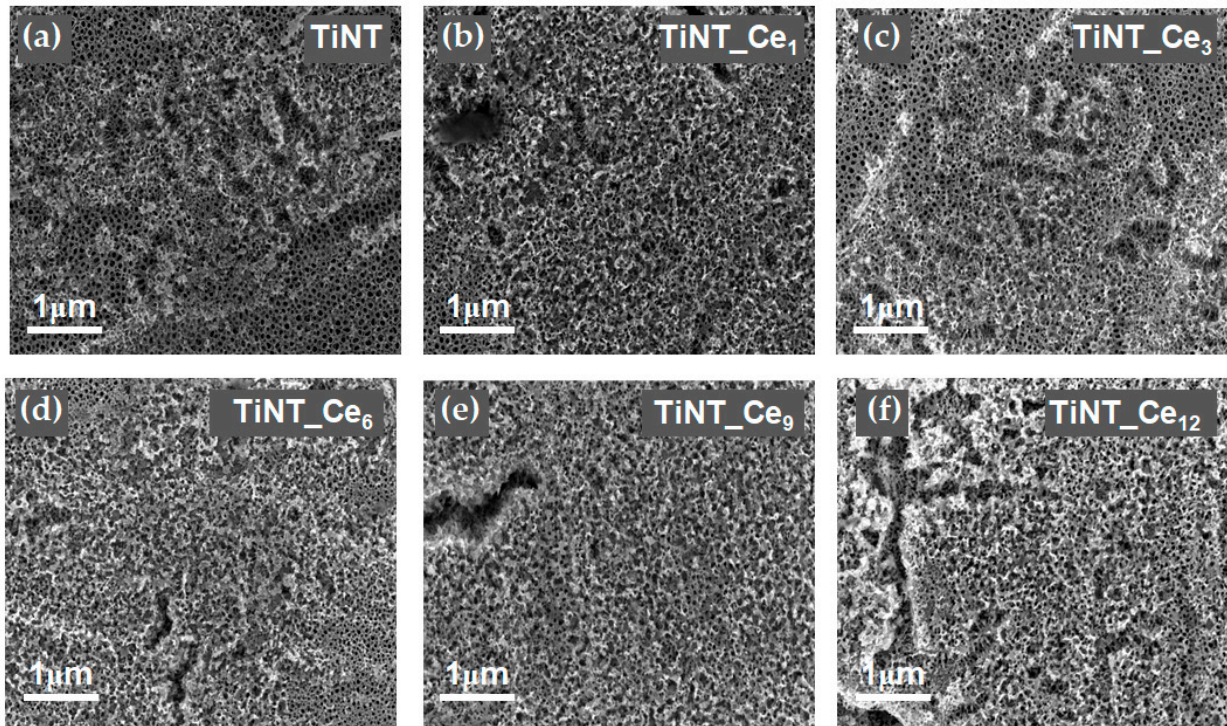
Figure 6. Top surface FE-SEM images of (**a**) TiO2 nanotube and (**b**–**f**) cerium-coated TiO2 nanotubes soaked in SBF 8 days at 37 °C showing the presence of HA precipitate covering the original open top nanostructure.
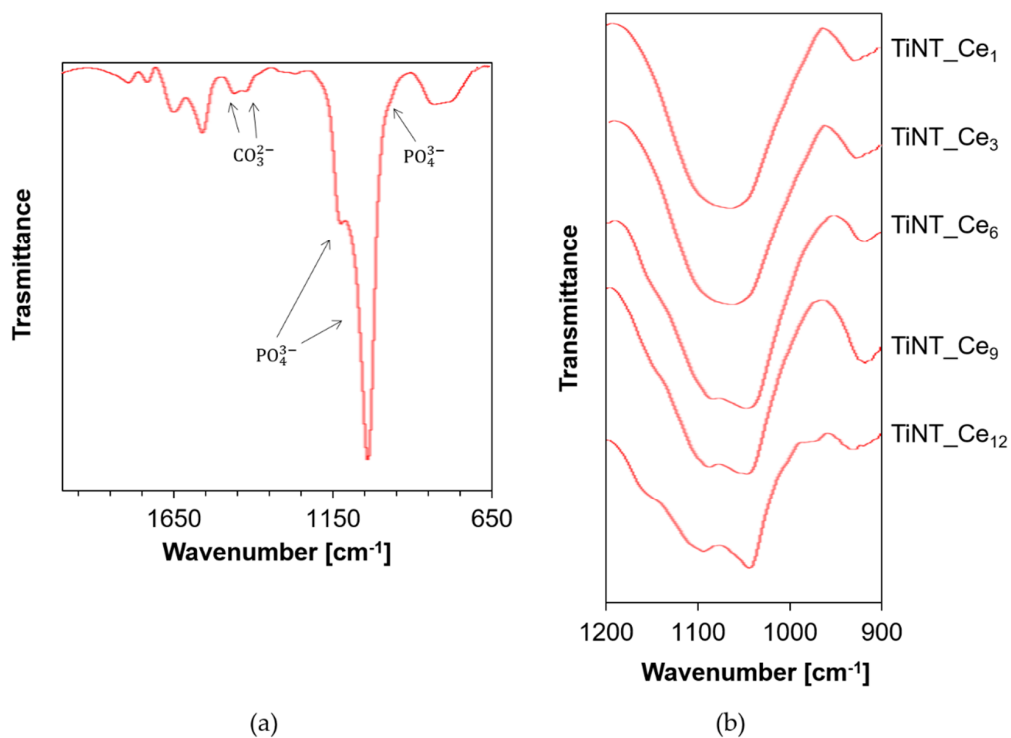
Figure 7. (**a**) ATR-FTIR spectra of TiNT_Ce$_{12}$ after 8 days soaking in SBF at 37 °C (**b**) ν_3 vibrational mode of PO$_4^{3-}$ was evidenced for the TiNT_Ce$_n$ samples.

4. Conclusions

Cerium-coated titanium nanotubes were prepared by coupling controlled anodic oxidation with a series on drop casting and annealing steps. The homogeneous distribution of the nanotubes and the typical open top topography was preserved even for the highest number of CeO_x depositions considered, without altering the original diameters and increasing the homogeneity of the surface. $TiNT\_Ce_n$ proved to have good corrosion resistance, with cerium exerting a protective action toward the active site on the titanium surface. All the samples showed similar wettability, slightly lower than that of pristine TiNTs. Nevertheless, a growing ability to induce early HA precipitation from SBF was observed as the cerium content of the surface increased. It was also observed that the HA deposited on samples in which the atomic percentage of cerium is higher than 4% ($TiNT\_Ce_6$) possessed a (poorly) crystalline form, indicative of a more advanced state of maturation and therefore of a potentially more rapid in vivo osseointegration process. Based on the data here discussed, $TiNT\_Ce_9$ (7% atomic percentage) can be considered as the most favorable, since its electrochemical properties and ability to induce HA maturation are comparable to those of $TiNT\_Ce_{12}$ while requiring fewer preparation steps. The influence of cerium content on cell adhesion and viability and its effective antibacterial and anti-inflammatory capabilities are currently under investigation to gain further insight into CeO_x-based materials properties. Nevertheless, the simple, easily scalable method here proposed stands as an interesting alternative for the improvement of titanium-based implants bioactivity.

Supplementary Materials: The following are available online at https://www.mdpi.com/2079-4991/11/2/445/s1, Figure S1: Image analysis of the FE-SEM micrographs for TiNT and $TiNT\_Ce_n$. Panels (a) and (b) show the original SEM output (in gray) partially superimposed onto the binarized image generated for the calculation. Panel c–h report the inner and outer diameter distribution for each sample. Figure S2: FE-SEM micrograph and EDS spectrum relative to the selected area. EDS was performed at 15 kV at the same magnification and corresponding total area for every sample; Figure S3: XPS O1s fitted spectra for (a) TiNT and (b–f) TiNT_Cen samples. Data were fitted with four components of about 530, 531.5, 533, and 534 eV that correspond to O2− of metal oxides, carbonyl oxygens, always present in samples prepared in air, hydroxyl groups (or chemisorbed water) and physisorbed water, respectively, Figure S4: XPS Ti2p fitted spectra for (a) TiNT and (b–f) TiNT_Cen samples, Figure S5: FE-SEM micrograph and EDS spectrum relative to the selected area. EDS was performed at 15 kV at the same magnification and corresponding total area for every sample, Table S1: Elemental composition (in atomic %) of TiNT and TiNT_Cen samples, Table S2: Elemental composition (in atomic %) of TiNT and $TiNT\_Ce_n$ samples after 8 days soaking in SBF at 37 °C.

Author Contributions: Conceptualization, S.D.S. and M.O.; data curation, S.D.S., G.S., M.M., G.I. and M.O.; formal analysis, S.D.S., G.S., G.I. and M.O.; funding acquisition, G.S. and M.O.; Investigation, S.D.S. and M.M.; methodology, F.P.; project administration, M.O.; writing—original draft, S.D.S.; writing—review and editing, G.S., G.I. and M.O. All authors have read and agreed to the published version of the manuscript.

Data Availability Statement: Not applicable.

Conflicts of Interest: The authors declare no conflict of interest.

References

1. Geetha, M.; Singh, A.K.; Asokamani, R.; Gogia, A.K. Ti based biomaterials, the ultimate choice for orthopaedic implants—A review. *Prog. Mater. Sci.* **2009**, *54*, 397–425. [CrossRef]
2. Raphel, J.; Holodniy, M.; Goodman, S.B.; Heilshorn, S.C. Multifunctional coatings to simultaneously promote osseointegration and prevent infection of orthopaedic implants. *Biomaterials* **2016**, *84*, 301–314. [CrossRef] [PubMed]

3. Grzeskowiak, R.M.; Schumacher, J.; Dhar, M.S.; Harper, D.P.; Mulon, P.Y.; Anderson, D.E. Bone and cartilage interfaces with orthopedic implants: A literature review. *Front. Surg.* **2020**, *7*, 601244. [CrossRef]

4. Bartkowiak, A.; Zarzycki, A.; Kac, S.; Perzanowski, M.; Marszalek, M. Mechanical properties of different nanopatterned TiO$_2$ substrates and their effect on hydrothermally synthesized bioactive hydroxyapatite coatings. *Materials* **2020**, *13*, 5290. [CrossRef]

5. Stepanovska, J.; Matejka, R.; Rosina, J.; Bacakova, L. The effect of various surface treatments of Ti$_6$Al$_4$V on the growth and osteogenic differentiation of adipose tissue-derived stem cells. *Coatings* **2020**, *10*, 762. [CrossRef]

6. Park, J.; Kim, Y.; Jang, J.; Kwon, T.; Bae, Y.; Suh, J. Effects of phosphoric acid treatment of titanium surfaces on surface properties, osteoblast response and removal of torque forces. *Acta Biomater.* **2010**, *6*, 1661–1670. [CrossRef] [PubMed]

7. Battocchio, C.; Concolato, S.; De Santis, S.; Pahlman, M.; Iuggi, G.; Santi, M.; Sotgiu, G.; Orsini, M. Chitosan functionalization of titanium and Ti$_6$Al$_4$V alloy with chloroacetic acid as linker agent. *Mater. Sci. Eng. C* **2019**, *99*, 1133–1140. [CrossRef]

8. Wehner, C.; Behm, C.; Husejnagic, S.; Moritz, A.; Rausch-Fan, X. Effect of Multi-Phosphonate Coating of Titanium Surfaces on Osteogenic Potential. *Materials* **2020**, *13*, 5777. [CrossRef]

9. Zhang, H.; Shi, X.; Tian, A.; Wang, L.; Liu, C. Electrochemical properties of Ti^{3+} doped Ag-Ti nanotube arrays coated with hydroxyapatite. *Appl. Surf. Sci.* **2018**, *436*, 579–584. [CrossRef]

10. Peng, Z.; Ni, J.; Zheng, K.; Shen, Y.; Wang, X.; He, G.; Jin, S.; Tang, T. Dual effects and mechanism of TiO$_2$ nanotube arrays in reducing bacterial colonization and enhancing C3H10T1/2 cell adhesion. *Int. J. Nanomed.* **2013**, *8*, 3093. [CrossRef]

11. Li, Y.; Yang, Y.; Li, R.; Tang, X.; Guo, D.; Qing, Y.; Qin, Y. Enhanced antibacterial properties of orthopedic implants by titanium nanotube surface modification: A review of current techniques. *Int. J. Nanomed.* **2019**, *14*, 7217–7236. [CrossRef]

12. Calıskan, N.; Bayram, C.; Erdal, E.; Karahaliloglu, Z.; Denkbaş, E.B. Titania nanotubes with adjustable dimensions for drug reservoir sites and enhanced cell adhesion. *Mater. Sci. Eng. C* **2014**, *35*, 100–105. [CrossRef] [PubMed]

13. Aw, M.S.; Addai-Mensah, J.; Losich, D. Polymer micelles for delayed release of therapeutics from drug-releasing surfaces with nanotubular structures. *Macromol. Biosci.* **2012**, *12*, 1048–1052. [CrossRef] [PubMed]

14. Williams, D.F. On the mechanisms of biocompatibility. *Biomaterials* **2008**, *29*, 2941–2953. [CrossRef] [PubMed]

15. Banfi, G.; Iorio, L.E.; Corsi, M.M. Oxidative stress, free radicals and bone remodeling. *Clinic. Chem. Lab. Med.* **2008**, *46*, 1550. [CrossRef]

16. Awad, N.K.; Edwards, S.L.; Morsi, Y.S. A review of TiO$_2$ NTs on Ti metal: Electrochemical synthesis, functionalization and potential use as bone implants. *Mater. Sci. Eng. C* **2017**, *76*, 1401–1412. [CrossRef]

17. Wojcieszak, D.; Mazur, M.; Kalisz, M.; Grobelny, M. Influence of Cu, Au and Ag on structural and surface properties of bioactive coatings based on titanium. *Mater. Sci. Eng. C* **2017**, *71*, 1115–1121. [CrossRef]

18. Lytkina, D.; Gutsalova, A.; Fedorishin, D.; Korotchenko, N.; Akhmedzhanov, R.; Kozik, V.; Kurzina, I. Synthesis and Properties of Zinc-Modified Hydroxyapatite. *J. Funct. Biomater.* **2020**, *11*, 10. [CrossRef]

19. Shimazaki, T.; Miyamoto, H.; Ando, Y.; Noda, I.; Yonekura, Y.; Kawano, S.; Miyazaki, M.; Mawatari, M.; Hotokebuchi, T. In vivo antibacterial and silver-releasing properties of novel thermal sprayed silver-containing hydroxyapatite coating. *J Biomed. Mater. Res. B Appl. Biomater.* **2010**, *92*, 386–389. [CrossRef] [PubMed]

20. Sedelnikova, M.B.; Komarova, E.G.; Sharkeev, Y.P.; Ugodchikova, A.V.; Tolkacheva, T.V.; Rau, J.V.; Buyko, E.E.; Ivanov, V.V.; Sheikin, V.V. Modification of titanium surface via Ag-, Sr- and Si-containing micro-arc calcium phosphate coating. *Bioact. Mater.* **2019**, *4*, 224–235. [CrossRef]

21. Ball, J.P.; Mound, B.A.; Monsalve, A.G.; Nino, J.C.; Allen, J.B. Biocompatibility evaluation of porous ceria foams for orthopedic tissue engineering. *J. Biomed. Mater. Res. Part A* **2015**, *103*, 8–15. [CrossRef]

22. Gravina, A.N.; Ruso, J.M.; Laiuppa, J.A.; Santillàn, G.; Marco-Brown, J.L.; D'Elia, N.L.; Messina, P.V. Striped, bioactive Ce–TiO$_2$ materials with peroxynitrite-scavenging activity. *J. Mater. Chem. B* **2014**, *2*, 834–845. [CrossRef] [PubMed]

23. Gravina, N.; Ruso, J.M.; Mbeh, D.A.; Yahia, L.; Sartuqui, J.; Messina, P.V. Effect of ceria on the organization and bio-ability of anatase fullerene-like crystals. *RSC Adv.* **2015**, *5*, 8077–8087. [CrossRef]

24. Baldim, V.; Bedioui, F.; Mignet, N.; Margaill, I.; Berret, J.-F. The enzyme-like catalytic activity of cerium oxide nanoparticles and its dependency on Ce^{3+} surface area concentration. *Nanoscale* **2018**, *10*, 6971–6980. [CrossRef] [PubMed]

25. Shoko, E.; Smith, M.F.; McKenzie, R.H. Charge distribution near bulk oxygen vacancies in cerium oxides. *J. Phys. Condens. Matter.* **2010**, *22*, 223201. [CrossRef] [PubMed]

26. Li, K.; Xie, Y.; You, M.; Huang, L.; Zheng, X. Plasma sprayed cerium oxide coating inhibits H$_2$O$_2$-induced oxidative stress and supports cell viability. *J. Mater. Sci. Mater. Med.* **2016**, *27*, 100. [CrossRef] [PubMed]

27. Gravina, A.N.; Rubert, A.A.; Bertuola, M.; Fernández Lorenzo de Mele, M. Bioactivity enhancement of cerium-containing titanium oxide nanotubes. Relationship between surface reactivity and nanostructuring process. *Surf. Coat. Technol.* **2019**, *378*, 124968. [CrossRef]

28. Zhang, J.H.; Zhu, Y.F. Synthesis and characterization of CeO$_2$-incorporated mesoporous calcium-silicate materials. *Micropor. Mesopor. Mat.* **2014**, *197*, 244–251. [CrossRef]

29. Nicolini, V.; Gambuzzi, E.; Malavasi, G.; Menabue, L.; Menziani, M.C.; Lusvardi, G.; Pedone, A.; Benedetti, F.; Luches, P.; D'Addato, S.; et al. Evidence of catalase mimetic activity in Ce^{3+}/Ce^{4+} doped bioactive glasses. *J. Phys. Chem. B* **2015**, *119*, 4009–4019. [CrossRef]

30. Mandoli, C.; Pagliari, F.; Pagliari, S.; Forte, G.; Di Nardo, P.; Licoccia, S.; Traversa, E. Stem cell aligned growth induced by CeO$_2$ nanoparticles in PLGA scaffolds with improved bioactivity for regenerative medicine. *Adv. Funct. Mater.* **2010**, *20*, 1617–1624. [CrossRef]

31. Li, X.; Qi, M.; Sun, X.; Weir, M.D.; Tay, F.R.; Oates, T.W.; Dong, B.; Zhou, Y.; Wang, L.; Xu, H.H.K. Surface treatments on titanium implants via nanostructured ceria for antibacterial and anti-inflammatory capabilities. *Acta Biomater.* **2019**, *94*, 627–643. [CrossRef]

32. You, M.; Li, K.; Xie, Y.; Huang, L.; Zheng, X. The Effects of Cerium Valence States at Cerium Oxide Coatings on the Responses of Bone Mesenchymal Stem Cells and Macrophages. *Biol. Trace Elem. Res.* **2017**, *179*, 259–270. [CrossRef]

33. Kokubo, T.; Takadama, H. How useful is SBF in predicting in vivo bone bioactivity? *Biomaterials* **2006**, *27*, 2907–2915. [CrossRef]

34. IInternational Standard ISO 23317:2014 Implants for Surgery—In Vitro Evaluation for Apatite-Forming Ability of Implant Materials. (2014). *ICS:11:040:040.* Available online: https://www.iso.org/standard/65054.html (accessed on 2 February 2021).

35. Park, J.; Bauer, S.; von der Mark, K.; Schmuki, P. Nanosize and vitality: TiO$_2$ nanotube diameter directs cell fate. *Nano Lett.* **2007**, 1686–1691. [CrossRef]

36. Zhou, Y.; Zhou, J. Ti/CeOx(111) interfaces studied by XPS and STM. *Surf. Sci.* **2012**, *606*, 749–753. [CrossRef]

37. Fang, J.; Bao, H.; He, B.; Wang, F.; Si, D.; Jiang, Z.; Pan, Z. Interfacial and Surface Structures of CeO$_2$–TiO$_2$ Mixed Oxides. *J. Phys. Chem. C* **2007**, *111*, 19078–19085. [CrossRef]

38. Moeini, S.S.; Battocchio, C.; Casciardi, S.; Luisetto, I.; Lupattelli, P.; Tofani, D.; Tuti, S. Oxidized Palladium Supported on Ceria Nanorods for Catalytic Aerobic Oxidation of Benzyl Alcohol to Benzaldehyde in Protic Solvents. *Catalysts* **2019**, *9*, 847. [CrossRef]

39. He, J.; Xu, Y.; Shao, P.; Yang, L.; Sun, Y.; Yang, Y.; Cui, F.; Wang, W. Modulation of coordinative unsaturation degree and valence state for cerium-based adsorbent to boost phosphate adsorption. *Chem. Eng. J.* **2020**, *394*, 124912. [CrossRef]

40. Gittens, R.A.; Scheideler, L.; Rupp, F.; Hyzy, S.L.; Geis-Gerstorfer, J.; Schwartz, Z.; Boyan, B.D. A Review on the Wettability of Dental Implant Surfaces II: Biological and Clinical Aspects. *Acta Biomater.* **2014**, *10*, 2907–2918. [CrossRef] [PubMed]

41. Lotsari, A.; Rajasekharan, A.K.; Halvarsson, M.; Andersson, M. Transformation of amorphous calcium phosphate to bone-like apatite. *Nat. Commun.* **2018**, *9*, 4170. [CrossRef] [PubMed]

42. Hench, L.L. Bioceramics: From concept to clinic. *J. Am. Ceram. Soc.* **1991**, *74*, 1487–1510. [CrossRef]

43. Iafisco, M.; Morales, J.G.; Hernández-Hernández, M.A.; García-Ruiz, J.M.; Roveri, N. Biomimetic Carbonate–Hydroxyapatite Nanocrystals Prepared by Vapor Diffusion. *Adv. Eng. Mater.* **2010**, *12*, B218–B223. [CrossRef]

44. Frank-Kamenetskaya, O.; Kol'tsov, A.; Kuz'mina, M.; Zorina, M.; Poritskaya, L. Ion substitutions and non-stoichiometry of carbonated apatite-(CaOH) synthesised by precipitation and hydrothermal methods. *J. Mol. Struct.* **2011**, *992*, 9–18. [CrossRef]

45. De Santis, S.; Sotgiu, G.; Crescenzi, A.; Taffon, C.; Felici, A.C.; Orsini, M. On the chemical composition of psammoma bodies microcalcifications in thyroid cancer tissues. *J. Pharmaceut. Biomed.* **2020**, *190*, 113534. [CrossRef] [PubMed]

46. Pleshko, N.; Boskey, A.; Mendelsohn, R. Novel infrared spectroscopic method for the determination of crystallinity of hydroxyapatite minerals. *Biophys. J.* **1991**, *60*, 786–793. [CrossRef]

47. Rey, C.; Combes, C.; Drouet, C.; Sfihi, H.; Barroug, A. Physico-chemical properties of nanocrystalline apatites: Implications for biominerals and biomaterials. *Mater. Sci. Eng. C* **2007**, *27*, 198–205. [CrossRef]